Geochemistry Geophysics Geosystems G3

Article
Volume 13, Number 1
21 February 2012
Q02009, doi:10.1029/2011GC003896
ISSN: 1525-2027

Published by AGU and the Geochemical Society

Continental delamination: Insights from laboratory models

Flora Bajolet
Dipartimento Scienze Geologiche, Università "Roma TRE," Largo S. L. Murialdo 1, I-00146 Rome, Italy (flora.bajolet@uniroma3.it)

Javier Galeano
Departamento Ciencia y Tecnología Aplicadas, EUIT Agrícola, Universidad Politécnica de Madrid, E-28040 Madrid, Spain

Francesca Funiciello
Dipartimento Scienze Geologiche, Università "Roma TRE," Largo S. L. Murialdo 1, I-00146 Rome, Italy

Monica Moroni
DICEA, Sapienza Università di Roma, via Eudossiana 18, I-00184 Rome, Italy

Ana-María Negredo
Departamento Física de la Tierra, Astronomía y Astrofísica I, and Instituto de Geociencias (CSIC-UCM), Facultad de Ciencias Físicas, Universidad Complutense de Madrid, E-28040 Madrid, Spain

Claudio Faccenna
Dipartimento Scienze Geologiche, Università "Roma TRE," Largo S. L. Murialdo 1, I-00146 Rome, Italy

[1] One of the major issues of the evolution of continental lithospheres is the detachment of the lithospheric mantle that may occur under certain conditions and its impact on the surface. In order to investigate the dynamics of continental delamination, we performed a parametric study using physically scaled laboratory models. The adopted setup is composed of a three-layers visco-elastic body (analog for upper crust, lower crust, lithospheric mantle) locally thickened/thinned to simulate a density anomaly (lithospheric root) and an adjacent weak zone, lying on a low viscosity material simulating the asthenosphere. The results emphasize the interplay between mantle flow, deformation, surface topography and plate motion during a three-phases process: (1) a slow initiation phase controlled by coupling and bending associated with contraction and dynamic subsidence, (2) lateral propagation of the delamination alongside with extension and a complex topographic signal controlled by coupling and buoyancy, while poloidal mantle flow develops around the tip of the delaminating lithospheric mantle, and (3) a late phase characterized by a counterflow that triggers retroward motion of the whole model. A semiquantitative study allows us to determine empirically two parameters: (1) an initiation parameter that constrains the propensity of the delamination to occur and correlates with the duration of the first stage, (2) a buoyancy parameter characterizing the delamination velocity during late stages and therefore its propensity to cease. Finally, we point out similarities and differences with the Sierra Nevada (California, USA) in terms of topography, deformation and timing of delamination.

Components: 10,900 words, 12 figures, 4 tables.

Keywords: Sierra Nevada; analog modeling; continental lithosphere; delamination; dynamic topography; mantle flow.

Index Terms: 8110 Tectonophysics: Continental tectonics: general (0905); 8120 Tectonophysics: Dynamics of lithosphere and mantle: general (1213).

Received 26 September 2011; **Revised** 9 January 2012; **Accepted** 17 January 2012; **Published** 21 February 2012.

Bajolet, F., J. Galeano, F. Funiciello, M. Moroni, A.-M. Negredo, and C. Faccenna (2012), Continental delamination: Insights from laboratory models, *Geochem. Geophys. Geosyst.*, *13*, Q02009, doi:10.1029/2011GC003896.

1. Introduction

[2] Continental delamination is presently one of the most discussed geodynamic processes due to its significant impact on the long-term behavior of the continental lithosphere. The concept of continental delamination was first introduced by *Bird* [1978, 1979], who proposed the hypothesis that along a tectonically stable area, the dense lithospheric mantle could peel away from the crust and sink into the asthenosphere. Delamination is permitted as soon as any process provides an elongated conduit connecting the underlying asthenosphere with the base of the continental crust. The delaminated mantle part of the lithosphere peels away as a coherent slice, without necessarily undergoing major internal deformation, and is replaced by buoyant asthenosphere. To avoid ambiguity, the term 'delamination' is used here to indicate the process that causes the asthenosphere to come into direct contact with the crust, and the hinge of delamination, where the lithosphere peels off the overlying crust, to migrate laterally. Others processes able to remove a part of the lithosphere such as convective removal of the lithospheric mantle developing from Rayleigh-Taylor instabilities [e.g., *Houseman et al.*, 1981; *England and Houseman*, 1989] are not considered here.

[3] Delamination has often been proposed to explain different observations such as regional uplift associated with alkaline volcanism, anomalously high heat flow and change of stress field toward extension in various geodynamic contexts: either near a plate boundary (western Mediterranean [*Channell and Mareschal*, 1989]; Alboran sea [*Seber et al.*, 1996; *Calvert et al.*, 2000; *Valera et al.*, 2008]); for intracontinental zones (Variscan belt [*Arnold et al.*, 2001]; Sierra Nevada in California [*Ducea and Saleeby*, 1998; *Zandt et al.*, 2004; *Le Pourhiet et al.*, 2006]); plateau interiors (Tibet [*Bird*, 1978]; Anatolia [*Göğüş and Pysklywec*, 2008a]; Colorado [*Bird*, 1979; *Lastowka et al.*, 2001; *Levander et al.*, 2011]); or in more complex areas exhibiting unusual intermediate depth seismicity (East Carpathians [*Gîrbacea and Frisch*, 1998; *Knapp et al.*, 2005; *Fillerup et al.*, 2010]).

[4] In spite of the popularity of continental delamination, its basic aspects remain poorly studied. For one part because most observables possibly indicating ongoing delamination are indirect ones (tomography, seismicity) [*Levander et al.*, 2011], and some surface features (tectonic, volcanism, topography) could be interpreted as subduction-related signals (i.e., slab roll-back, slab break-off). Moreover, few physical-numerical models have been developed [e.g., *Schott and Schmeling*, 1998; *Morency and Doin*, 2004; *Göğüş and Pysklywec*, 2008b; *Valera et al.*, 2008, 2011; *Faccenda et al.*, 2009]. Although these models successfully capture the main features of delamination, they have to deal with difficulties such as numerical instabilities associated with fast deforming bodies and with strong lateral contrasts of viscosity. Unlike subduction, which has been investigated by numerous laboratory studies over the last two decades [e.g., *Jacoby*, 1980; *Kincaid and Olson*, 1987; *Griffiths et al.*, 1995; *Guillou-Frottier et al.*, 1995; *Faccenna et al.*, 1996, 1999; *Funiciello et al.*, 2003, 2004, 2008; *Schellart*, 2004], or convective removal [*Pysklywec and Cruden*, 2004], very few attempts to reproduce continental delamination with analog models have been made [*Chemenda et al.*, 2000; *Göğüş et al.*, 2011].

[5] The main purpose of this study is to investigate the dynamics of continental delamination with laboratory models exploring the influence of various parameters (initial structure, rheological properties), and the relationships between deep dynamics (i.e., mantle circulation), surface deformation (i.e., deformation, isostatic reequilibration, dynamic topography), and plate motion.

2. Experimental Setup

[6] Delamination is reproduced in the laboratory using a thin sheet three-layers model (lithosphere), lying on top of a low-viscosity glucose syrup simulating the asthenospheric mantle (Figure 1). From top to bottom, the lithospheric sheet is composed of (1) visco-elastic silicone putty simulating the upper crust, (2) high-viscosity glucose syrup simulating

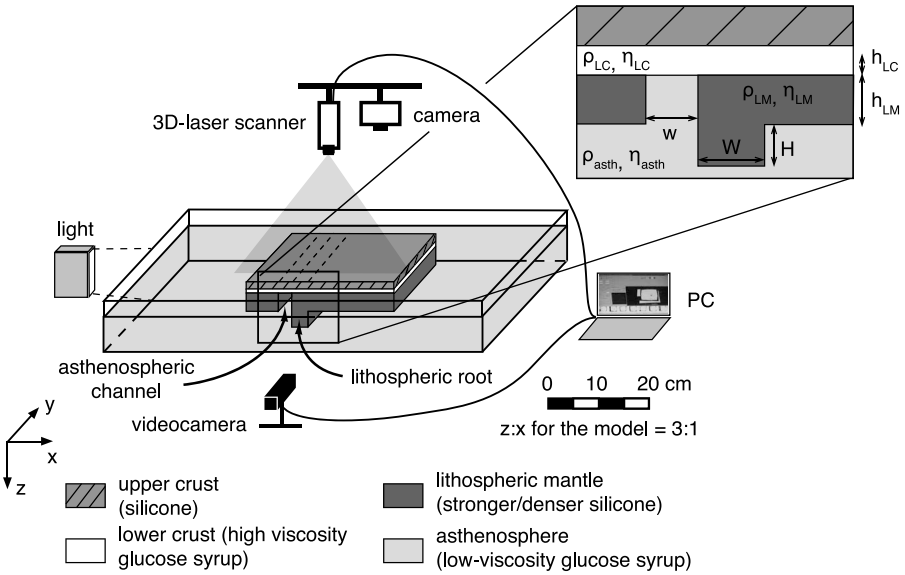

Figure 1. Experimental setup. Material properties are given in Table 1, and settings for each experiment in Table 3.

the viscous lower crust, (3) strong and dense viscoelastic silicone, analog of the lithospheric mantle (Table 1). The selected asthenospheric mantle is a Newtonian fluid whose viscosity allows us to obtain laminar flow in the limit of a small Reynolds number.

[7] The three-layered sheet is located in the center of a large Plexiglas tank (75 × 25 × 25 cm^3), whose bottom mimics the 660 km discontinuity, and is free to move in all directions (free boundary conditions). The distance between the plate and box sides is set large enough to minimize possible boundary effects [*Funiciello et al.*, 2006].

[8] This experimental setting is properly scaled for normal gravity field to simulate the competition between acting gravitational and viscous resistive forces stored within the mantle and the lithosphere [e.g., *Weijermars and Schmeling*, 1986; *Davy and Cobbold*, 1991]. The density and the viscosity ratios between the lithosphere and asthenosphere range between 1.01 and 1.02 and 400 and 3000, respectively. The length scale factor is fixed to 1.2×10^{-7} so that 1 cm in the models corresponds to 83 km in nature. Further details on experimental parameters and scaling relationships can be found in Table 2. The adopted setup implies the following assumptions, and consequent limitations, that are detailed in the work of *Funiciello et al.* [2003]: (1) isothermal system, (2) constant viscosity and density over the depth of the individual layers, (3) lack of global background mantle flow, (4) 660 km discontinuity as an impermeable barrier. In contrast with *Göğüş et al.* [2011], we do not impose any convergence, nor manually trigger initiation of delamination. Delamination is spontaneously enhanced by the adopted ad hoc initial condition which, in analogy with previous numerical models [*Schott and Schmeling*, 1998; *Valera et al.*, 2008, 2011], includes a zone of thicker lithospheric mantle (orogenic root, 1.04 cm thick in the reference experiment) adjacent to a weak zone represented by an asthenospheric channel (absence of lithospheric mantle; Figure 1). This configuration enables the asthenosphere upwelling to replace the

Table 1. Material Properties[a]

Material	Density (kg m^{-3})	Viscosity (Pa s^{-1})
Silicone 4 (upper crust)	1422	5.10^4
Silicone 7 (lithospheric mantle)	1476	1.10^5
Silicone 2 (light lithospheric mantle)	1456	6.10^4
Silicone 1 (very light lithospheric mantle)	1438	7.2×10^4
Intermediate syrup (asthenosphere)	1428	22
High viscosity syrup (lower crust)	1442	168
Very high viscosity syrup (lower crust experiment DEL23)	1455	425

[a]Viscosities are given for room temperature (22°C) and an experimental strain rate of 10^{-2} s^{-1} (scaled for nature).

Table 2. Scaling of Parameters for the Reference Experiment

	Parameter	Nature	Model
g	Gravitational acceleration (m s^{-2})	9.81	9.81
Thickness[a]			
h_l	Continental lithosphere (m)	100000	0.012
h_{asth}	Upper mantle asthenosphere (m)	660000	0.11
Density			
ρ_l	Continental lithosphere (kg m^3)	3200	1457
ρ_{asth}	Upper mantle asthenosphere (kg m^3)	3220	1428–1442
ρ_l / ρ_{um}	Density ratio	0.99	1.02–1.01
Viscosity			
η_l	Continental lithosphere (Pa s^{-1})	10^{23}	7×10^4
η_{asth}	Upper mantle asthenosphere (Pa s^{-1})	10^{21}	22–168
η_l / η_{um}	Viscosity ratio	10^2	4×10^2–3×10^3
	Dimensionless Parameters		**Equivalence Model-Nature**
$t°$	Characteristic time: $(t_{model}/t_{nature}) = (\Delta\rho g h)_{lith\ nature}/(\Delta\rho g h)_{lith\ model} \times (\eta_{l\ model}/\eta_{l\ nature})$		4.02×10^{-12} 1 $min_{model} \rightarrow 0.473$ My_{nature} 1 $h_{model} \rightarrow 28.4$ My_{nature}
$U°$	Characteristic velocity: $(U_{model}/U_{nature}) = t_{nature}/t_{model} \times L_{model}/L_{nature}$		29829 1 cm h^{-1} $_{model} \rightarrow 0.29$ cm y^{-1} $_{nature}$

[a]Scale factor for length $L_{model}/L_{nature} = 1.2 \times 10^{-7}$.

delaminated lithospheric mantle. A similar setting has also been adopted in the numerical models of *Göğüş and Pysklywec* [2008b], who considered a flat geometry of the lithospheric mantle, but imposed a local density increase of 100 kg m^{-3}, producing a negative buoyancy similar to our orogenic root. The presence of a local weakened zone is fundamental to trigger delamination in nature. This is usually explained as likely related to the presence of free water, which would decrease the pore pressure allowing a reduction in the brittle strength [*Schott and Schmeling*, 1998], or thermally active areas in response to active mantle upwelling. This weak zone is spontaneously created only in the model developed by *Morency and Doin* [2004] where strong localized thinning of the lithospheric mantle leads to the formation of an "asthenospheric conduit."

[9] Each model is monitored over its entire duration using a sequence of digital pictures taken in lateral and top views. We also record the evolution of the surface topography with a 3D-laser scanner (Real Scan USB) whose precision is 0.1 mm, corresponding to 830 m in nature. The evolution of delamination is monitored by Feature Tracking (FT) image analysis technique on representative experiments. In order to adopt the FT for our models, the glucose syrup is previously seeded with bright reflecting air micro-bubbles used as passive tracers. These bubbles have a diameter less than 1 mm, and consequently its possible influence on the density/viscosity is negligible. Images of the micro-bubbles are recorded by a CCD camera, set to acquire about 2 frames per second in lateral view. FT algorithms provide sparse velocity vectors with application points coincident with pixel luminosity intensity gradients characterizing the passive tracers seeding the mantle. This technique permits to obtain a Lagrangian description of the observed velocity field, which is then used to reconstruct instantaneous and time-averaged Eulerian velocity maps (modulus, x-y components, streamlines) through a resampling procedure [see *Funiciello et al.*, 2006, and references therein].

3. Experimental Results

[10] Our models were performed to provide new insights into the mechanical/dynamic behavior of the lithosphere in a delamination process. In particular, we intend to describe and quantify the spatial and temporal evolution of the mantle circulation induced by delamination and the related surface response. Fourteen models out of 26 (Table 3) have been selected to illustrate the influence of (1) plate thickness, (2) plate viscosity, (3) plate density, (4) presence/absence/size of the asthenospheric channel, (5) presence/absence/size of the lithospheric root, (6) asthenosphere viscosity on the delamination process.

Table 3. Experimental Parameters for Each Experiment[a]

Experiment	Plates (Size, Silicones)	Asthenospheric Channel Width (w)	Orogenic Root Width (W)	Layers Thickness
DEL10	UC (sil. 4): 30 × 18 cm^2 LM (sil. 7): 30 × 14 cm^2	2 cm	3 cm	UC: 0.375 cm LC: 0.2 cm LM: 0.78 cm Root: 1.04 cm
DEL11	UC (sil. 4): 30 × 18 cm^2 LM (sil. 7): 30 × 14 cm^2	***4 cm***	3 cm	UC: 0.38 cm LC: 0.2 cm LM: 0.665 cm Root: 1.04 cm
DEL12	UC (sil. 4): 30 × 18 cm^2 LM (sil. 7): 30 × 14 cm^2	2 cm	3 cm	UC: 0.37 cm LC: 0.2 cm LM: 0.775 cm ***Root: 0.55 cm***
DEL13	UC (sil. 4): 30 × 18 cm^2 LM (sil. 7): 30 × 14 cm^2	***1 cm***	3 cm	UC: 0.325 cm LC: 0.2 cm LM: 0.6 cm Root: 1.025 cm
DEL14	UC (sil. 4): 30 × 18 cm^2 LM (sil. 7): 30 × 14 cm^2	2 cm	3 cm	UC: 0.35 cm ***LC: 0.4 cm*** LM: 0.65 cm Root: 0.975 cm
DEL15	UC (sil. 4): 30 × 18 cm^2 LM (sil. 7): 30 × 14 cm^2	2 cm	***1 cm***	UC: 0.36 cm LC: 0.2 cm LM: 0.675 cm Root: 0.975 cm
DEL16	UC (sil. 4): 30 × 18 cm^2 LM (sil. 7): 30 × 14 cm^2	2 cm	***No orogenic root***	UC: 0.275 cm LC: 0.2 cm LM: 0.65 cm
DEL17	UC (sil. 4): 30 × 18 cm^2 LM (sil. 7): 30 × 14 cm^2	2 cm	***No orogenic root***	UC: 0.275 cm LC: 0.2 cm LM: 0.68 cm
DEL18	UC (sil. 4): 30 × 18 cm^2 LM ***(sil. 1)***: 30 × 14 cm^2	2 cm	3 cm	UC: 0.35 cm LC: 0.2 cm LM: 0.675 cm Root: 1.0 cm
DEL19	UC (sil. 4): 30 × 18 cm^2 LM ***(sil. 2)***: 30 × 14 cm^2	2 cm	3 cm	UC: 0.325 cm LC: 0.2 cm LM: 0.725 cm Root: 0.970 cm
DEL20	UC (sil. 4): 30 × 18 cm^2 LM (sil. 7): 30 × 14 cm^2 ***Asth.: high viscosity syrup***	2 cm	3 cm	UC: 0.340 cm LC: 0.2 cm LM: 0.720 cm Root: 0.940 cm
DEL21	UC (sil. 4): 30 × 18 cm^2 LM (sil.7): 30 × 14 cm^2	***No asthenospheric. channel***	***No orogenic root***	UC: 0.40 cm LC: 0.2 cm LM: 0.730 cm
DEL22	UC (sil. 4): 30 × 18 cm^2 LM (sil.7): 30 × 14 cm^2	***No asthenospheric. channel***	3 cm	UC: 0.320 cm LC: 0.2 cm LM: 0.760 cm Root: 0.950 cm
DEL23	UC (sil. 4): 30 × 18 cm^2 LM (sil.7): 30 × 14 cm^2	***No asthenospheric. channel***	***No orogenic root***	UC: 0.325 cm ***LC: 0.2 cm very high viscosity syrup*** LM: 0.660 cm
DEL24	UC (sil. 4): **30 × 25 cm^2** LM (sil.7): **30 × 24.5 cm^2**	***No asthenospheric. channel***	***No orogenic root***	UC: 0.350 cm LC: 0.2 cm LM: 0.770 cm

[a]UC: upper crust; LC: lower crust; LM: lithospheric mantle; Asth.: asthenosphere. Values in bold italic are the parameters varying compared to the reference case (DEL10). In a few experiments (DEL21, 22, 23), the lithospheric mantle tends to detach from the lower crust along the borders parallel to the length of the model. This is due to the fact that in this area, the layer of lower crust is in contact with the asthenosphere, thus creating a "false" asthenospheric channel. In experiment DEL24, the layer of silicone simulating the lithospheric mantle is larger avoiding the contact. In this case, there is no delamination.

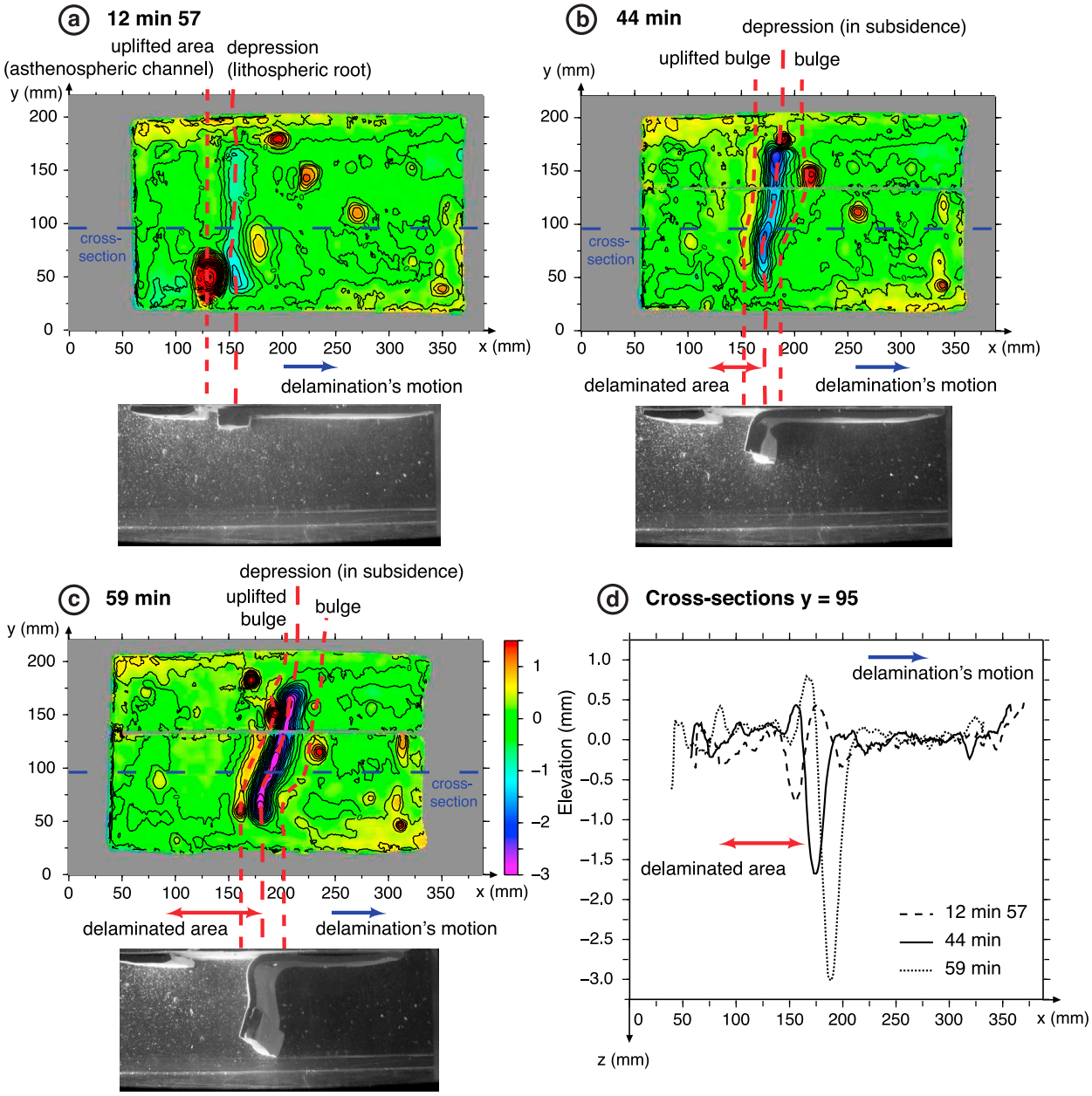

Figure 2. Side view photos and surface topography for the reference experiment (DEL10) at three stages of the delamination process: (a) 12 min 57s during initiation phase, (b) 44 min at the transition between main and final phase, (c) 59 min during final phase, with (d) corresponding cross-sections taken along the reference dotted blue line. The high (red) circular zones are air bubbles trapped between the layers during the construction of the model. Later experiments free of that experimental bias showed that it does not affect significantly the delamination process.

3.1. Evolution of the Reference Experiment (DEL 10)

[11] All the performed experiments show a typical sequence of deformation, starting from spontaneous delamination to the arrival of lithospheric mantle to the bottom of the box. In this section, we describe the typical evolution of the delamination process as recorded for the reference model DEL10. DEL10 is characterized by thicknesses of 0.375 cm, 0.2 cm and 0.78 cm for the upper crust, the lower crust and the lithospheric mantle, respectively. It includes a zone of 1.04 cm thick lithospheric mantle simulating the orogenic root. The other parameters are listed in Table 3. The proward direction is defined as the direction of migration of the delamination (toward the right in all the figures), and retroward direction corresponds to the opposite sense (toward

Table 4. Characteristic Values of Duration and Physical Parameters for Each Experiment[a]

Experiment	Difference With Reference Experiment	Duration of Initiation t	Duration of Main Phase	w_c (cm)	Duration of Final Stage	Root Pull F_{rp} ($\times 10^{-4}$ N)	Initiation Parameter I ($\times 10^{-7}$ s^7 m^{-3})	Buoyancy Parameter B ($\times 10^{-10}$ m^4 s^4 kg^{-1})	Mean Velocity During Stokes' Phase V ($\times 10^{-5}$ m s^{-1})
DEL10	Reference experiment	30 min (14.2 My)	4 min (34 min after the beginning of the experiment) (1.9 My)	4.8	27 min (12.8 My)	11.46	6.02	6.20	6.13
DEL11	Asthenospheric channel twice wider	25 min (11.8 My)	0 (25 min)	4.6	23 min (10.9 My)	9.77	16.57	5.29	9.85
DEL12	Lithospheric root half thick	60 min (28.4 My)	24.9 min (84.9 min) (11.8 My)	4.4	18.1 min (8.6 My)	6.02	3.23	3.26	4.13
DEL13	Asthenospheric channel twice narrower	30 min (14.2 My)	17.8 min (47.8 min) (8.4 My)	4.5	22.2 min (10.5 My)	8.69	5.01	4.70	7.15
DEL14	Lower crust twice thicker	15 min (7.1 My)	5 min (20 min) (2.4 My)	4.9	14 min (6.6 My)	8.95	16.26	9.69	16.6
DEL15	Lithospheric root 3 times narrower	50 min (23.6 My)	22 min (72 min) (10.4 My)	5.1	20 min (9.5 My)	3.10	2.51	1.68	4.02
DEL16	No orogenic root	45 min (21.3 My)	26 min (71 min) (12.3 My)	Variable along the width of the model	17 min (8.0 My)				Variable along the width of the model
DEL17	No orogenic root	60 min (28.4 My)	37 min (97 min) (17.5 My)	4.7	17 min (8.0 My)				Variable along the width of the model
DEL18	Density contrast 4.8 times smaller	No delamination				1.99	0.070	1.07	
DEL19	Density contrast 2.4 times smaller	1h 45 min (49.7 My)	5.5 min (110.5 min) (2.6 My)	3.7	39.5 min (18.7 My)	5.80	2.15	3.14	4.98
DEL20	Asthenosphere 10 times more viscous	2h 20 min (66.2 My)	15.9 min (155.9 min) (7.5 My)	4.3	74.1 min (35.0 My)	6.77	0.30	0.48	1.87
DEL21	No asthenospheric channel, no orogenic root	Detachment by setup bias							
DEL22	No asthesnospheric channel	Detachment by setup bias							

Table 4. (continued)

Experiment	Difference With Reference Experiment	Duration of Initiation t	Duration of Main Phase	w_c (cm)	Duration of Final Stage	Root Pull F_{rp} ($\times 10^{-4}$ N)	Initiation Parameter I ($\times 10^{-7}$ s^7 m^{-3})	Buoyancy Parameter B ($\times 10^{-10}$ m^4 s^4 kg^{-1})	Mean Velocity During Stokes' Phase V ($\times 10^{-5}$ m s^{-1})
DEL23	No asthenospheric channel, no orogenic root, lower crust more viscous	Detachment by setup bias							
DEL24	No asthenospheric channel, no orogenic root, larger plates	No delamination							

[a]Durations of characteristic phases are given in minutes with the corresponding scaled time for nature (in My). Main phase is defined as the time span between the end of initiation and the onset of retroward motion of the plate, the final phase from this change in kinematics until the DLM touches the bottom of the box. w_c is the width of the asthenospheric channel at the transition between main and final phase. For experiments DEL16 and DEL17, in the absence of lithospheric root, the shape of the delamination hinge is highly sinuous, with very variable velocities of delamination along the width of the model.

the part of the model that does not delaminate, i.e., left in the figures).

3.1.1. Initiation of Delamination

[12] At the beginning of the experiment, the area above the asthenospheric channel is 0.1 to 0.2 mm higher than the unperturbed area due to the absence of lithospheric mantle, and the area above the lithospheric root is 0.3 mm lower (Figures 2a and 2d). The edge of the unstable thickened lithospheric mantle slowly starts to peel away from the overlying lower crust alongside the length of the asthenospheric channel and displaces underlying mantle material proward (Figure 2a). The amount of time necessary to initiate this process is 30 min (corresponding to 14.2 My in nature) in the reference experiment (Table 4). Concurrently, the difference of pressure at the base of the sinking lithospheric mantle and in the asthenospheric channel produces a clockwise return flow that injects asthenospheric material into the lower crust toward the lithospheric root. This flow remains very modest during all the initiation with a maximum velocity of 3.6 cm h^{-1} (Figure 3a). A small amount of extension parallel to the direction of delamination affects the area above the asthenospheric channel, while the rest of the model is globally in contraction, which is stronger above the lithospheric root (Figure 4a). The depression caused by the pull of the thickened lithospheric mantle progressively narrows and deepens up to 0.9 mm. As subsidence is deforming the model, two bulges due to bending form, one at each side of the depression (i.e., each side of the lithospheric root). They are ca. 0.1 mm higher than the average elevation of the model (Figures 2a and 2d). Figure 5 shows the evolution of the elevation for the uplifted bulge located above the asthenospheric channel, and for the depression migrating with the delamination hinge. Figure 6 shows the evolution of horizontal velocity of both the dynamic depression, that corresponds to the velocity of delamination (in the plate reference frame), and of the whole model (in a fixed external reference frame).

3.1.2. Main Phase of Delamination

[13] Once the lithospheric mantle decouples from the crust, the hinge of the delamination migrates progressively proward and the dip of the delaminated lithospheric mantle (DLM) increases (Figure 3b). As the DLM rolls back in the proward direction, the poloidal clockwise flow centered beneath the tip of the slab enhances the ascent of

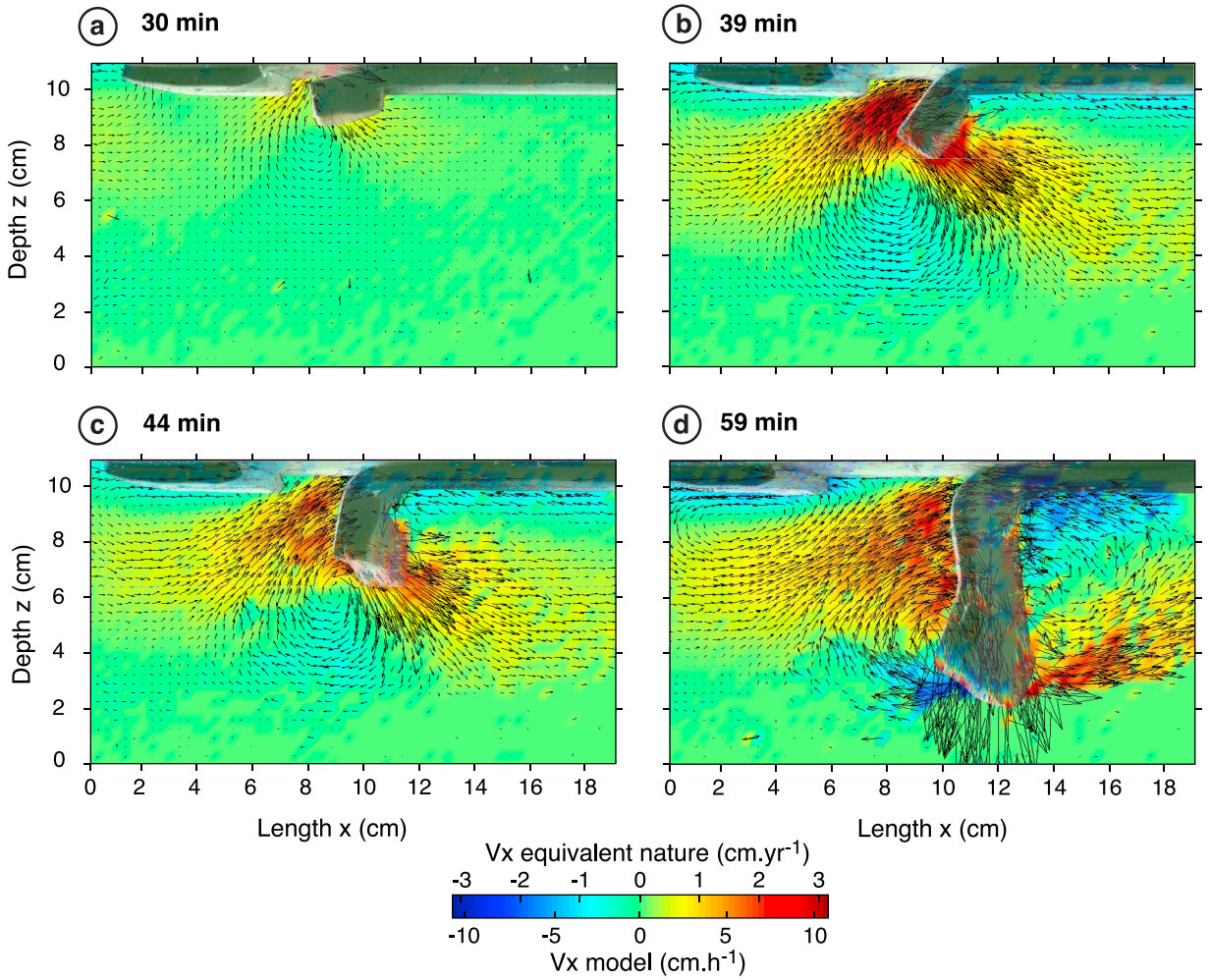

Figure 3. Velocity field (lateral view) for experiment DEL10 at four different stages of the delamination: (a) 30 min just after initiation, (b) 39 min at the end of the main phase of delamination, (c) 44 min at the change in dynamic with strong increase in retroward motion of the model, and (d) 59 min during the last phase of delamination, just before the DLM reaches the bottom of the box. Color scale represents the velocity in the x direction (length, positive in the proward direction). Shadowed images underline the position of the model.

asthenosphere, which replaces the DLM. Maximum velocities of 10.8 cm h^{-1} are reached soon after the end of the main phase, at 39 min (Figure 3b). Sinking and proward motion of the DLM enlarge the asthenospheric channel and an ascending asthenospheric counterflow directed retroward grows (Figure 3c). The initial topographic signal (composed of the depression flanked by the two bulges) moves laterally following the delamination's propagation with a velocity reaching 8 cm h^{-1} at 33 min (equivalent to 2.4 cm yr^{-1} in nature, Figure 6a), and increases in amplitude. The bulge situated toward the asthenospheric channel is more uplifted than the one on the other side (reaching respectively 0.3 and 0.2 mm; Figures 2b and 2d) due to the impingement of the ascending asthenospheric material against the base of the crust. The increased bending of the plate causes the formation of a second area of extension above the smaller flexural bulge (Figure 4b). The area where the lithospheric mantle is removed is also uplifted by 0.1 to 0.3 mm (Figures 2a, 2b, and 2d). This elevated zone will remain permanently until the end of the experiment, whereas high and low areas moving with the delamination are the transient, dynamic response of the system.

3.1.3. Final Stage

[14] Around 4 min after delamination initiation, i.e., 34 min after the beginning of the experiment, the width of the delaminated area reaches a critical value of ca. 4.5 cm (Table 4). The pull induced by the DLM triggers the rapid retroward motion of the plate that sharply accelerates up to 12 cm h^{-1} at the

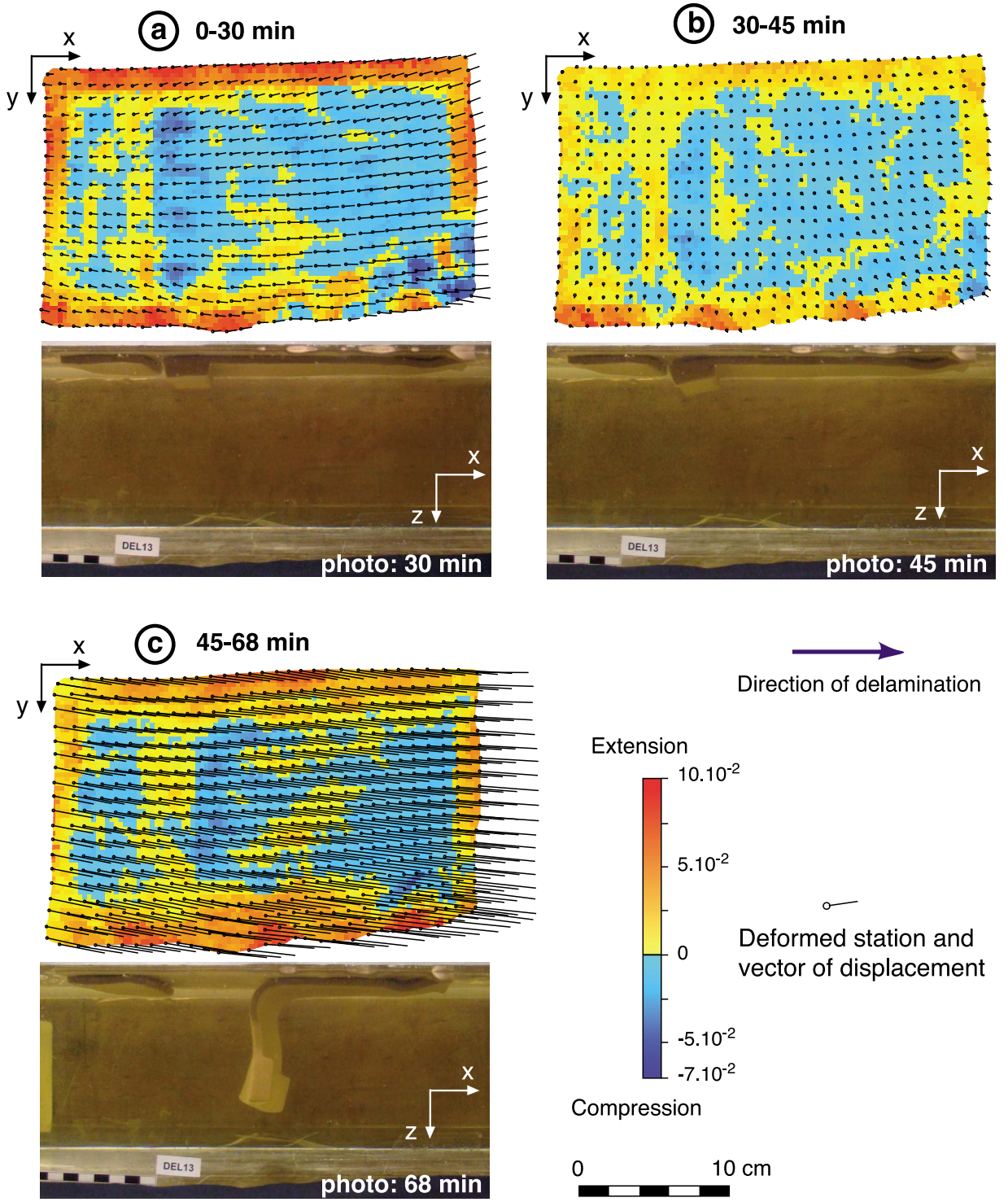

Figure 4. 2D finite strain map of the upper crust (top view) and corresponding side view photos at 3 different stages of the delamination for experiment DEL13: (a) initiation between 0 and 30 min, (b) main phase between 30 and 45 min, and (c) final phase between 45 and 68 min. Finite strain is computed with SSPX software [*Cardozo and Allmendinger*, 2009]. Initial and final coordinates of reference points drawn on the upper silicone are transformed into a displacement gradient tensor from which is calculated the strain gradient tensor. The deformation field is then computed with a grid-nearest neighbor method.

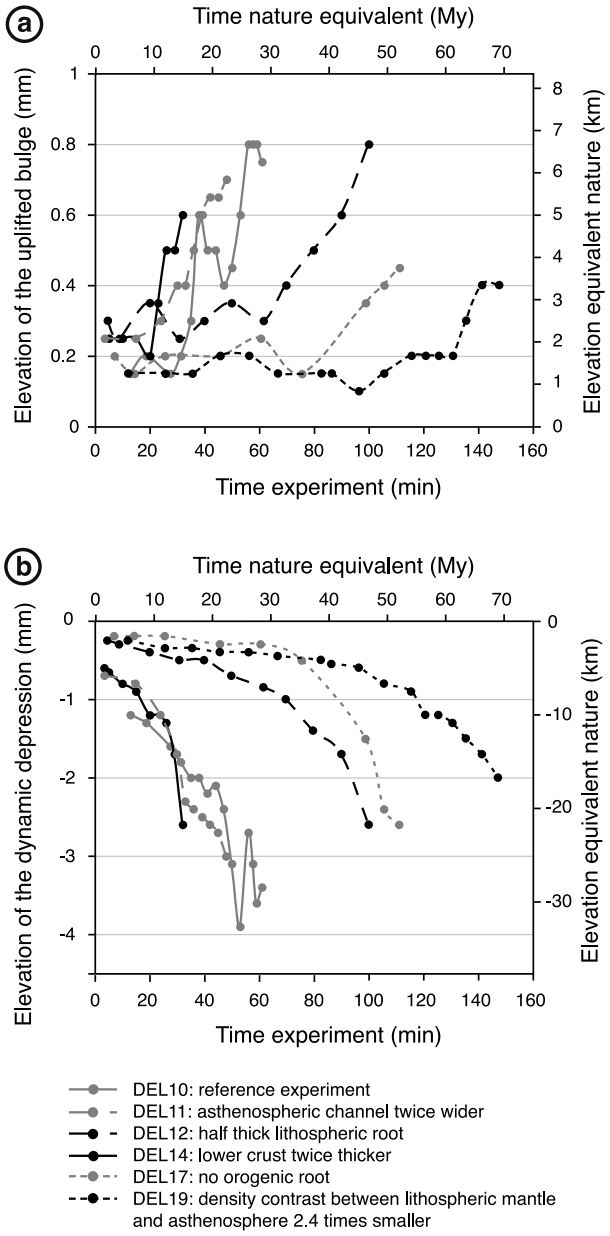

Figure 5. Evolution through time of (a) the amplitude of elevation for the uplifted bulge and (b) depression migrating with the delamination's hinge in the plate reference frame (most significant experiments). The curves stop just before the DLM touches the bottom of the box (upper/lower mantle boundary).

end of the experiment (3.5 cm yr^{-1} in nature, Figure 6b), and enhances the efficiency of the asthenospheric counterclockwise flow (Figure 3b). The DLM's proward motion stops although delamination proceeds: the DLM roughly remains in a fixed position with respect to an external fixed reference frame, and delaminates near vertically. The mantle circulation associated with this final stage is thus characterized by the coeval flow of two advection cells, a clockwise cell to the left of DLM and a counterclockwise cell to the right (counterflow).

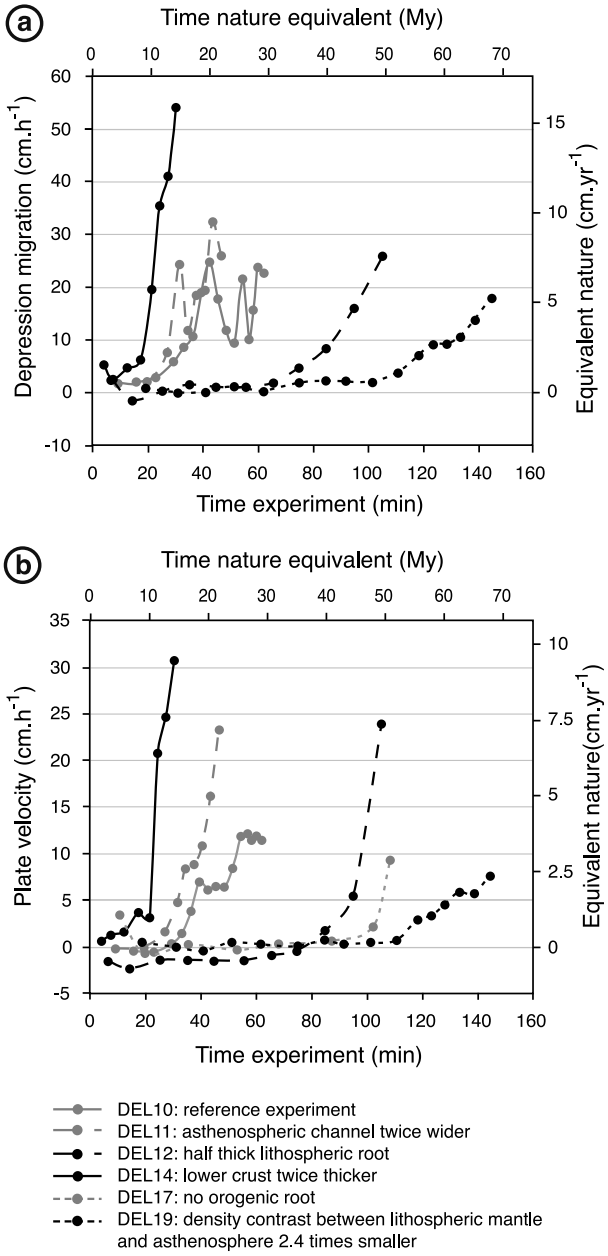

Figure 6. Evolution of (a) the horizontal velocity of the dynamic depression in the plate referential and (b) the whole model in a fixed external reference frame. The displacement of the dynamic depression follows the delamination front and can be assimilated with the horizontal velocity of delamination. Delamination during experiment DEL17 (without orogenic root) is very irregular and it is therefore difficult to measure the displacement of the dynamic depression at the delamination's hinge.

[15] Consequently to the near-vertical position of the DLM, the hinge of delamination, the associated surface deformation and the topographic signal also remain fixed with respect to an external reference frame. However, they still move proward in the plate's reference frame, with a maximum velocity of 23 cm h^{-1} at the end of the experiment (6.8 cm yr^{-1} in nature, Figure 6a). Increase in amplitude of both the depression and uplifted bulge continues until the DLM approaches the bottom of the box (Figures 2c, 2d, and 5). Similarly, the surface above the delaminated area continues to widen and uplift up to 0.2 to 0.3 mm as previously (Figure 2d). Zones of extension (associated with both bulges) and contraction (associated with the dynamic depression) follow the delamination's hinge as elastic deformation. The resulting finite deformation for the whole duration of the final phase shows widening of extension both above the delaminated area and the flexural bulge. However, approximately half the delaminated area has undergone finite compression (Figure 4c). A part of the deformation is elastic and thus transient, but the model is also durably deformed with 6% of shortening accumulated in the whole lithosphere at the end of the experiment.

3.2. Sensitivity Analysis

[16] We performed a parametric study to test how the initial geometrical configuration and rheological properties of the lithosphere can influence the evolution of delamination. The main features characterizing the delamination process are invariant for all the experiments, but the timescale, mantle flow velocity and amplitude of the surface features depend on the adopted parameters.

[17] Key parameters determining the occurrence and timing of the first phase of delamination are the thickness of the lower crust (i.e., degree of coupling between lower crust and lithospheric mantle), and the width of the asthenospheric channel. Delamination starts earlier and proceeds faster when the lower crust is thicker, and/or the asthenospheric channel is wider (compare in Figures 5 and 6 DEL10 with DEL11 and DEL14, Table 4). Thickness of the orogenic root, alongside with density contrast between the lithospheric mantle and asthenosphere has also an impact on delamination velocity, especially in the initiation phase (compare in Figures 5 and 6 DEL10 and DEL19, Table 4). If the density contrast is very small (<7 kg m^{-3}), the delamination does not initiate (Table 3, DEL18 not detailed here). A viscosity contrast one order of magnitude lower slows down the whole process, initiation as well as main and final phases of delamination (Tables 3 and 4, DEL20 not detailed here).

[18] Although the global pattern of mantle flow is stable whatever the parameters are, the timing of the different phases and flow velocities vary. If the asthenospheric channel is initially two times larger (4 cm instead of 2 cm, DEL 11, Figure 7a), delamination is slightly faster during the whole modeling evolution (Table 4). More precisely, mantle flow is slower during the main phase of delamination (with a maximum of 8.1 cm h^{-1} against 10.8 cm h^{-1} for reference experiment; Figure 7b), followed by a faster final phase (9 cm h^{-1} against 7.2 cm h^{-1}, Figure 7d). When the orogenic root is half thick (0.55 cm instead of 1.04 cm, DEL12, Figures 7e–7h), we do not observe clear distinct phases but rather a continuous increase in flow velocity, more significant after the retroward plate motion has started (Figures 7g and 7h). However, this result must be taken with caution given that in this experiment, the delamination front is twisted and does not allow a good view for mantle flow record.

[19] The topographic signal results from the interplay between different parameters, with a dominant role played by the gravitational instability of the lithospheric root. The amplitude of the topography (both for the depression and the uplifted bulge) is higher for a thick and dense lithospheric root, which therefore creates a stronger relief (Figure 5, compare DEL10, DEL12, DEL 17 and DEL 19). On the contrary, a lower viscosity contrast between lithosphere and asthenosphere results in lower amplitude of topography (Table 3, DEL20 not detailed here).

[20] Geometry and propagation of delamination is controlled by the presence/absence and size of the orogenic root. In experiments where the lithospheric root is absent (Table 3 and Figure 5, DEL17 and DEL16, not detailed here), delamination begins strongly delocalized along the asthenospheric channel and, afterwards, irregularly propagates in several directions. As a consequence, the topographic signal following the delamination is also heterogeneous in shape and amplitude.

4. Discussion

[21] All the parameters discussed below are listed with symbols and units in the Notation section.

4.1. Forces at Work During Delamination

[22] A typical feature of delamination, compared to convective removal, is that the lithospheric mantle

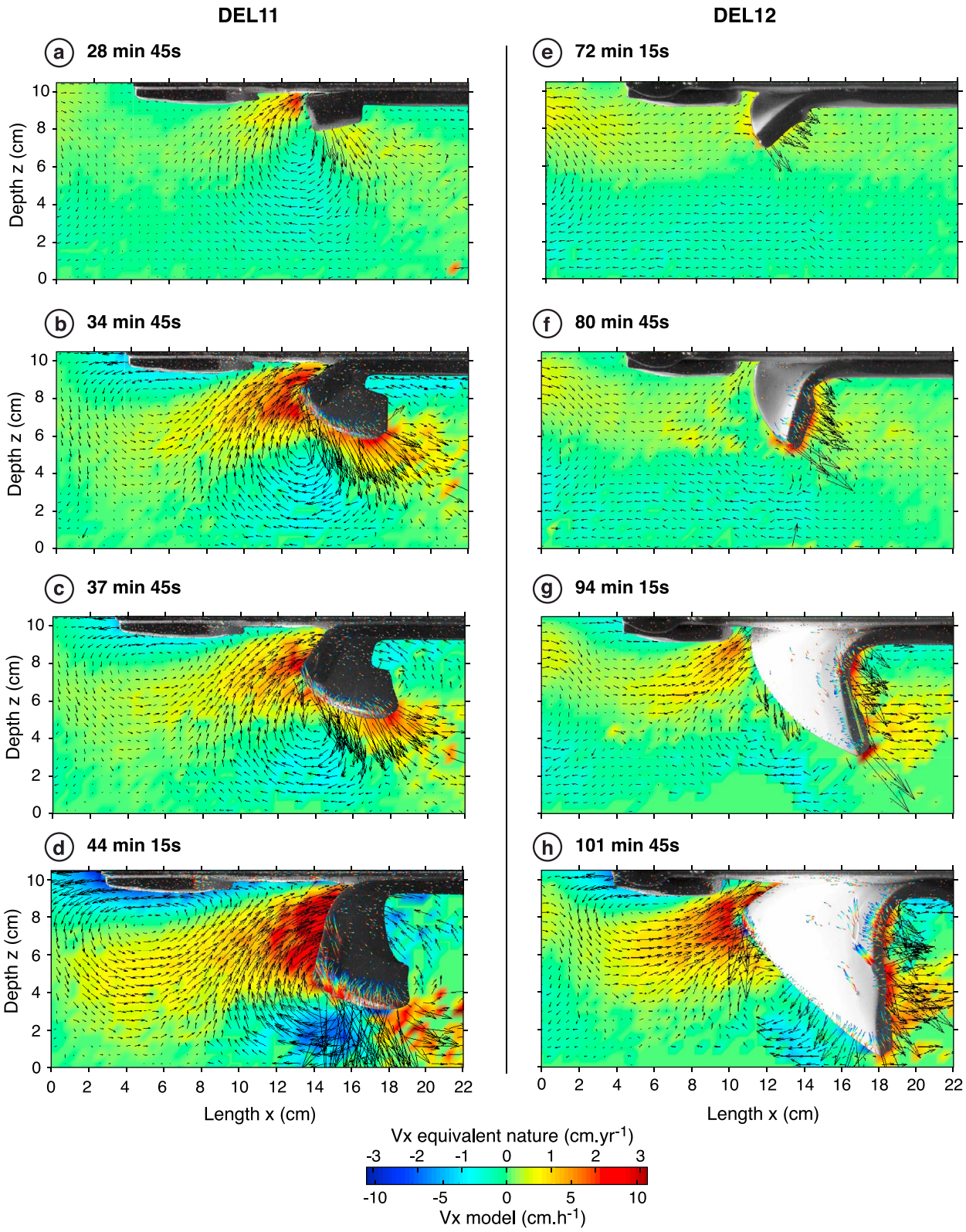

Figure 7. Velocity field for experiments (a–d) DEL11 and (e–h) DEL12 presented as for Figure 3 (see caption).

delaminates coherently, with little internal deformation and with a geometry comparable to that of a subducting lithosphere. Thus, the following analysis of forces acting during the delamination process is partly inferred from previous studies on subduction [e.g., *Forsyth and Uyeda*, 1975; *Turcotte and Schubert*, 1982; *Conrad and Hager*, 1999; *Funiciello et al.*, 2003; *Lallemand et al.*, 2008].

[23] The main driving force is the gravitational instability generated by the presence of the lithospheric root that progressively pulls down the lithospheric mantle. The root pull (F_{rp}) increases with time as more lithospheric mantle is delaminated. In analogy with the slab pull [e.g., *Forsyth and Uyeda*, 1975; *McKenzie*, 1977; *Davies*, 1980], our root pull force can be expressed as

$$F_{rp} = \Delta\rho g h_{LM} WH \quad (1)$$

where $\Delta\rho$ is the density contrast between the lithospheric mantle and the asthenosphere, g the gravity acceleration, h_{LM} is the thickness of the delaminated lithospheric mantle and W and H the width and thickness of the lithospheric root respectively.

[24] The resisting forces include the shear resistance at the lower crust/lithospheric mantle boundary, the bending resistance, and the asthenosphere resistance at the interface with the DLM. First, the lithospheric mantle has to overcome the coupling (i.e., the shear resistance) with the lower crust. The shear stress at the base of the lower crust τ_{LC} is proportional to the shear rate $\dot{\gamma}$ and the viscosity of the lower crust η_{LC},

$$\tau_{LC} = \dot{\gamma}\,\eta_{LC} \quad (2)$$

The lower crust deforms by a combination of Couette and Poiseuille flow. However, side view photos show a pattern closer to Couette flow's geometry at the base of the lower crust, consistent with the deformation observed in numerical models [*Le Pourhiet et al.*, 2006]. Therefore, we will approximate the shear rate at the first order as Couette flow in a Newtonian fluid so that

$$\dot{\gamma} = v/h_{LC} \quad (3)$$

where v is the velocity in the lower crust and h_{LC} its thickness. Expressions (2) and (3) give

$$\tau_{LC} = v\,\eta_{LC}/h_{LC} \quad (4)$$

The delamination process requires bending of the lithospheric mantle. Following *Turcotte and Schubert* [1982], the force necessary to bend a viscous layer can be approximated by

$$R_b \approx V_d h_{LM}^3 \eta_{LM}/r^3 \quad (5)$$

where V_d is the velocity of delamination, η_{LM} and r the viscosity and radius of curvature of the lithospheric mantle respectively.

[25] The displaced asthenosphere also exerts a viscous resistance on the DLM at its interface. For subduction, this resistance has been solved with fluid dynamics equations for the case of a stationary slab [*Turcotte and Schubert*, 1982]. Following the simplification adopted by *Funiciello et al.* [2003], we will only estimate the order of magnitude. At the first order, the viscous shear resistance is proportional to the asthenosphere viscosity η_{asth} and velocity of delamination V_d

$$R_{asth} \propto \eta_{asth} V_d \quad (6)$$

Acceleration of delamination with time implies a faster increase of the driving force (root pull) compared to the resisting forces. Indeed, the bending resistance decreases rapidly as it is inversely proportional to the cube of the radius of curvature expressed as the deviation of the initial straight shape. The shear resistance at the base of the lower crust and the viscous resistance of the asthenosphere, tough increasing with the velocity in the lower crust and the velocity of delamination respectively, do not compensate for the augmentation of the root pull force. In the following section, we examine the evolution of the forces at work with time and their influence on the observables (timing, velocities, topography) and attempt to further quantify the delamination process.

4.2. Dynamics of Delamination and Surface Response

[26] The initial configuration is unstable due to the negative buoyancy of the lithospheric mantle. Conditions for initiation include a sufficient root pull: if $F_{rp} < 2 \times 10^{-4}$ N (experiment DEL18) the process does not start within the time span tested in laboratory (4 h equivalent to 113.5 My). The mantle flow generated in the asthenospheric channel is very modest and is due to the difference of pressure between the asthenospheric channel and the base of the heavy lithospheric root. Injection of asthenospheric material at the extremity of the lithospheric root causes a viscosity decrease in the area previously occupied by the lower crust. Progressive sinking of the root enlarges the

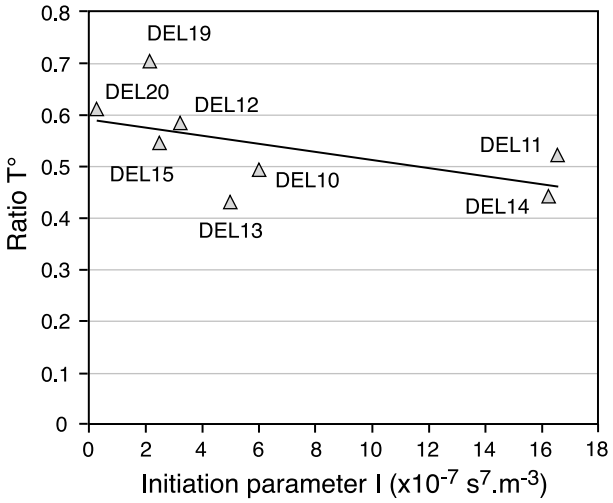

Figure 8. Plot of the initiation parameter (I) versus the ratio between the time required for initiation of delamination and the total duration of the experiment ($T°$) with best fit regression line. The regression coefficient is -7.9×10^4.

conduit. Consequently, the shear resistance τ_{LC} (equation (4)) is reduced with relative increase of the root pull force's efficiency. This is indeed confirmed in experiment DEL14: when the lower crust is twice thicker, the time required for initiation is twice shorter (Table 4 and Figures 5 and 6). A wider asthenospheric channel (DEL11) allows for a stronger initial mantle flow that also reduces slightly the duration of initiation phase (Table 4 and Figures 5 and 6). In order to determine the main parameters controlling the initiation phase, we consider two parameters: the ratio $T°$ between the time required for initiation (t) and the total duration of the experiment (T):

$$T^\circ = t/T \tag{7}$$

and an initiation parameter (I) representing the ratio of driving forces over resisting forces acting during initiation such as

$$I = F_{rp}/\tau_{LC} R_b R_{asth} \tag{8}$$

I will successfully represent the possibility for delamination to initiate if it correlates well with $T°$. We can therefore try to adjust its expression empirically. In equations (4), (5) and (6), we observe that τ_{LC}, R_b and R_{asth} are proportional to η_{LC}/h_{LC}, η_{asth} and $h_{LM}^3\eta_{LM}$, respectively, then

$$I \propto F_{rp} h_{LC}/\eta_{LC}\eta_{asth} h_{LM}{}^3 \eta_{LM} \tag{9}$$

Moreover, the width of the asthenospheric channel, not taken into account in the force balance analysis, is a parameter enhancing the velocity of the initiation phase and hence can be placed at the numerator. The best fit between I and $T°$ is obtained by adding a factor $\Delta\rho^2$ that highlights the strong dependency of the initiation duration on the density contrast so that

$$I \propto F_{rp}\Delta\rho^2 h_{LC} w/\eta_{LC}\eta_{asth} h_{LM\eta LM}^3 \tag{10}$$

Figure 8 shows a good linearly inverse correlation between I and $T°$, highlighting how I and, in turn, the interplay between its constitutive parameters, reasonably characterizes the possibility for the delamination to initiate.

[27] At the onset of the experiments, the zone above the asthenospheric channel undergoes fast isostatic reequilibration and is uplifted due to the absence of lithospheric mantle. The observed initial value of this uplifted zone ranges between 0.1 and 0.3 mm (corresponding to 0.6 to 1.8 km) and reasonably fits the prediction by Airy model (i.e., 0.24 mm; Figure 2a). The depression above the lithospheric root has also a flexural bending component, as the upper and lower crusts are deflected downward by the root pull (dynamic effect). Once decoupling has started, the DLM bends preferentially in the region just behind the lithospheric root, where the resistance is smaller. Indeed, the bending resistance increases as the cube of the thickness (equation (5)), preventing any important bending of the lithospheric root. Finally, the increase of the root pull force becomes high enough to control the system dynamics. The transition between the bending-dominated phase and the root pull-dominated phase is easily identifiable by plotting the vertical position and velocity of the tip of the DLM against time (Figure 9). At some point, the vertical velocity increases almost linearly with time, adopting a Stokes flow-like law, also observed in numerical simulations [*Le Pourhiet et al.*, 2006] (Figure 9b). The predominance of the root pull force can be further verified by comparing the mean vertical velocity during this period to a buoyancy parameter, B, (Figure 10) defined as

$$B = F_{rp}/\tau_{LC} R_{asth} \tag{11}$$

that we simplify, in the same way as for I, as

$$B \propto F_{rp} h_{LC}/\eta_{LC}\eta_{asth} \tag{12}$$

B includes the root pull force over the asthenosphere viscosity, characteristic of a Stokes sinker. However, the good correlation between B and the mean vertical velocity (Figure 9) is obtained only introducing the ratio of lower crust thickness over its

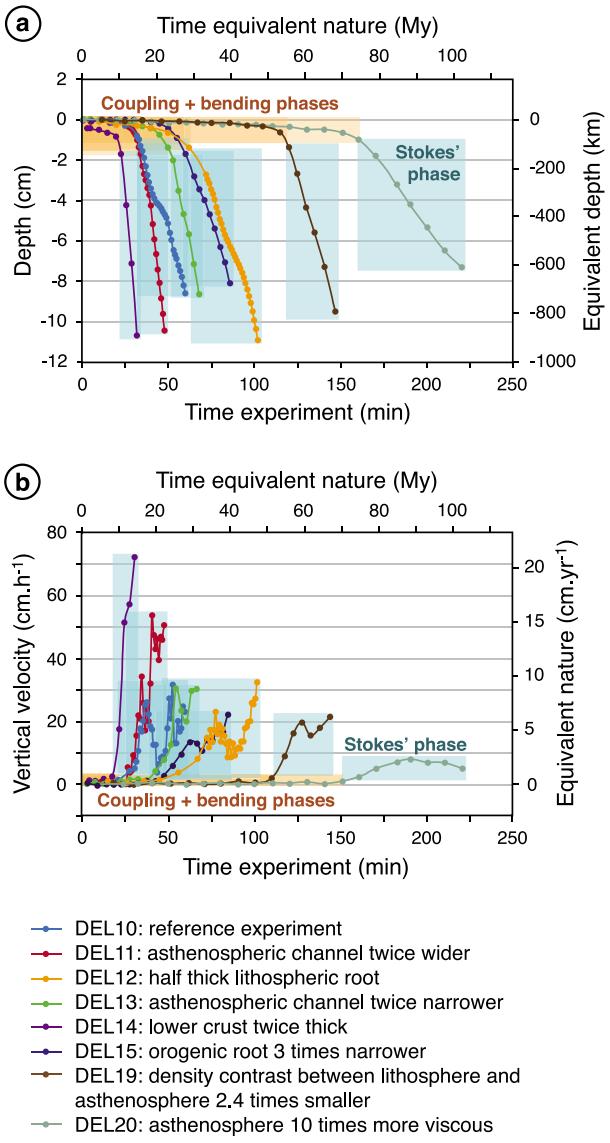

Figure 9. Evolution of (a) the vertical position and (b) vertical velocity of the tip of the DLM through time. First stages dominated by coupling and bending are highlighted in orange, last stage dominated by root pull and characterized by a sinking similar to Stokes flow law is highlighted in blue. Curves stop just before the DLM touches the bottom of the box (upper/lower mantle boundary). The slight decrease of the vertical velocity visible on a few curves (Figure 9b) is due to transitory periods of uneven delamination (lateral variations, with one side delaminating faster than the other).

viscosity, proportional to the shear resistance τ_{LC}. This implies that the coupling between the lower crust and the lithospheric mantle remains a determining force all along the delamination process.

[28] Concurrently to the delamination acceleration, the amount of subsidence progressively increases and the maximum locus of depression migrates laterally following the delamination hinge motion (Figures 2b and 2c). This observable shows that a large part of the recorded topographic signal can be attributed to dynamic topography. The mantle flow also speeds up, generating fast asthenospheric upwelling. Therefore, there is a positive feedback between the induced mantle circulation and sinking of the DLM (progression of the delamination). The ascending asthenospheric flow is also responsible for the larger uplift of the bulge flanking the retroward side of the dynamic depression, with an elevation up to 0.7 mm higher than the proward bulge, which is only generated by bending (Figures 2c, 2d, and 11). Uplift of the delaminated area is thus partly isostatic (as observed at the beginning of experiments above the initial asthenospheric channel), and partly dynamically supported by the mantle flow.

[29] In summary, velocity of propagation, amplitude of the dynamic topography and plate motion are correlated with delamination hinge motion (Figures 5 and 6) and with sinking of the DLM, and, therefore, with mantle flow velocity. The initiation phase is mainly controlled by the density contrast between the DLM and asthenosphere (equation (10)), the shear resistance at the base of the lower crust, the bending resistance and width of the asthenospheric channel. During the main phase, slow migration of the delamination front starts with active poloidal flow (Figures 3, 6a, and 9). The onset of the final phase can be defined when the delaminated area reaches a critical value of

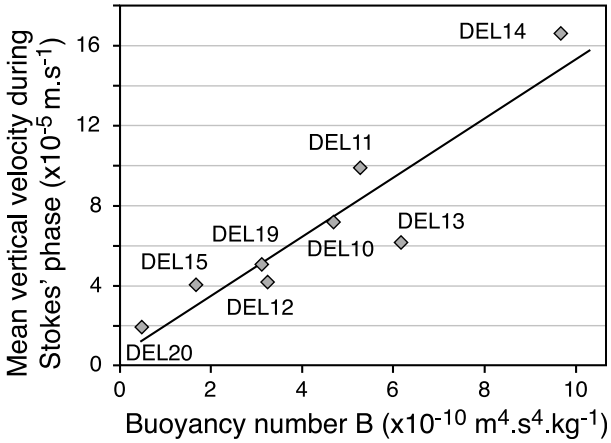

Figure 10. Graph highlighting the correlation between the mean vertical velocity during Stokes' phase (V) and the buoyancy parameter (B) (root-pull dominated phase) with best fit regression line. The regression coefficient is 57.6.

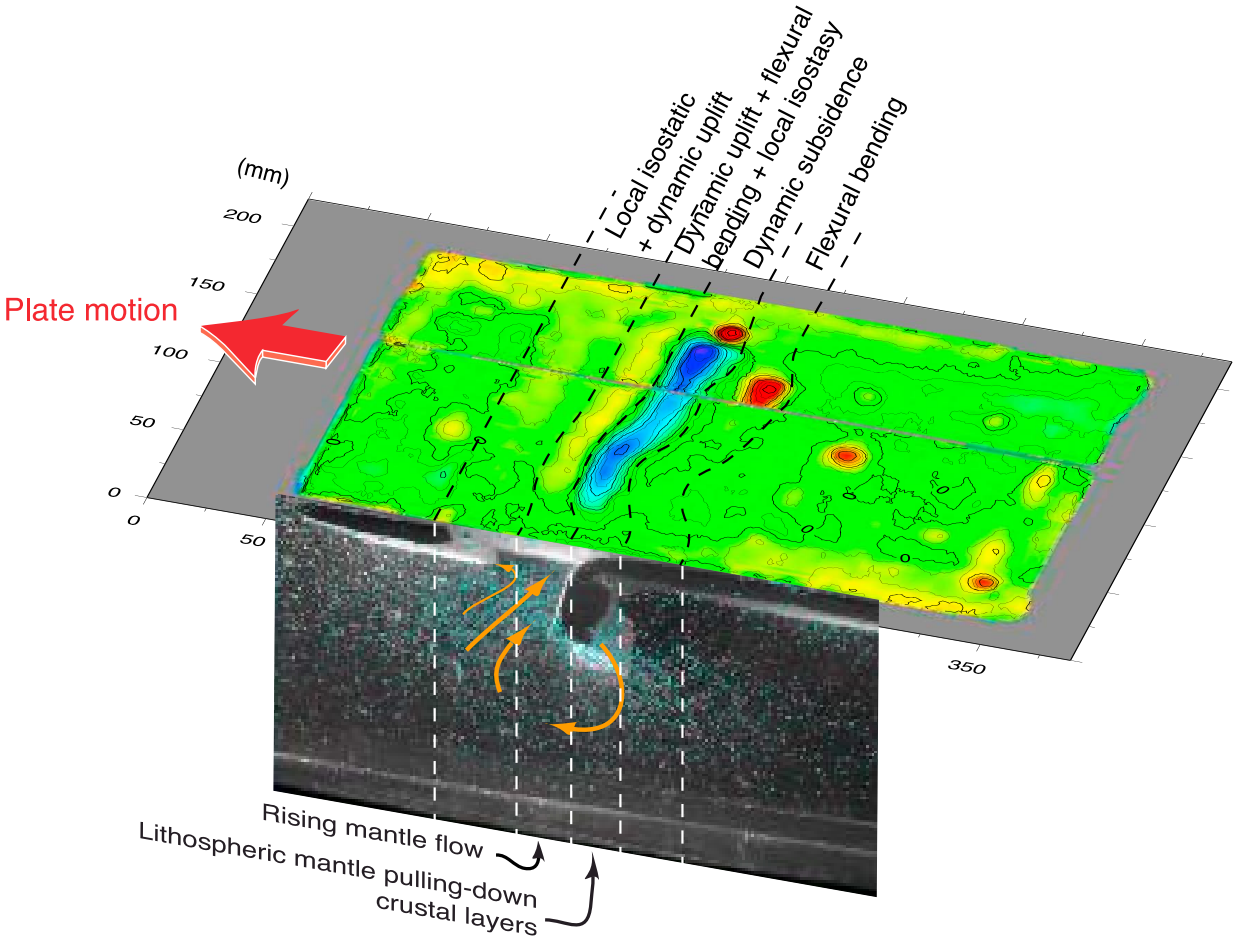

Figure 11. Reconstruction of the relationships between mantle flow and surface topography during delamination (reference experiment DEL10 at 18 min 40s).

~4.5 cm. The counterflow triggers rapid plate motion and faster delamination, correlated with strong increase of dynamic topography (Table 4 and Figures 5, 6, and 11). Ultimately, delamination is controlled by buoyancy force and shear resistance, close to a Stokes sinker behavior. The transition between initiation (characterized by parameter I) and Stokes phases (characterized by parameter B) can occur either during main or final phase (Figure 9).

[30] One may restrict the conditions required for delamination by plotting B versus I (Figure 12). If I is too small, delamination will not start (experiment DEL18). Moreover, in a natural system, we expect the process to freeze if the motion is too slow (i.e., if B is too small) event though initiation was possible. Most probably, the velocity of delamination in experiment DEL20 is too low to be sustained in a real convective-advective system, as heat transport will be faster than material motion. We can define a range for the critical values of I and B below which delamination will not start (I_c) or will stop (B_c). We find $6.99 \times 10^{-9} < I_c < 2.97 \times 10^{-8}$ and $4.80 \times 10^{-11} < B_c < 1.68 \times 10^{-10}$ (Figure 12). The viscoelastic behavior of our analog materials rules out the possibility for break-off of the DLM. However, detachment of the root and/or part of the DLM will reduce the root pull force and could also cause cessation of the delamination.

4.3. Comparison With Previous Modeling Results

[31] Numerical studies dealing with delamination introduced the calculation of the topographic response using a wide range of approaches. *Bird and Baumgardner* [1981] introduced the calculated dynamic pressure in the equation of elastic bending of the crust. *Schott and Schmeling* [1998] computed the topography calculating the vertical

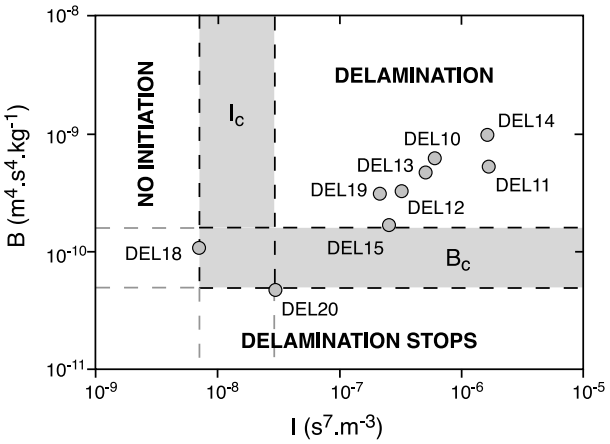

Figure 12. Plot of the initiation parameter (I) versus the buoyancy parameter (B). Domains where delamination does not occur, stops during the process, or continues are constrained by experiments DEL18, DEL20, and DEL15. Shaded areas represent the uncertainties on the critical values I_c and B_c delimiting the different domains.

normal stresses exerted on the model surface. *Göğüş and Pysklywec* [2008b] included a free top surface, where topography develops as the model evolves. And, finally, *Valera et al.* [2011] introduced a thin upper layer of low density and viscosity to allow the top of the crust to behave as a free surface. The results of our laboratory models are reasonably comparable to the numerical models by *Göğüş and Pysklywec* [2008b] because in both cases a significant amount of lateral migration of the delamination hinge is reproduced, whereas the other studies predict small to moderate (less than about 400 km) hinge migration.

[32] The typical signal characterized by the migrating pattern of subsidence and uplift - the former caused by the sinking of the delaminated lithospheric mantle, the latter due to asthenospheric upwelling - is consistently reproduced in both numerical and laboratory approaches. However, in the work of *Göğüş and Pysklywec* [2008b] the amplitude of the highest bulge is smaller than in our experiments. This can be explained as their weak zone consists of normally buoyant lithospheric mantle, which acts as a barrier and slows downs the ascent of asthenosphere. On the contrary, the buoyant "asthenospheric conduit" introduced in our setup enables the direct impingement of the asthenosphere into the base of the crust. In both the work of *Göğüş and Pysklywec* [2008b] and our models, a high amplitude of the negative deflection is obtained, related to the extra negative buoyancy imposed to initiate the delamination process. In contrast, the models by *Schott and Schmeling* [1998] and *Valera et al.* [2008, 2011] predict a much smaller long-term subsidence because DLM buoyancy, which is only thermally induced, diminishes with time as heated from thermal diffusion. *Valera et al.* [2011] highlight the sensitivity to the initial crustal structure and show that in some cases of initially orogenic crust, the sinking of DLM drags down the lower crust so that the positively buoyant thickened crust locally overcomes the effect of negative buoyancy of DLM, resulting in overall surface uplift. In our experiments, the lower crust acting as a decoupling layer is partly dragged downward into the asthenosphere alongside with the DLM, while another part remains in place beneath the upper crust. The interface between the remaining lower crust and the asthenosphere is very irregular, probably disturbed by the mantle flow. For natural systems, the dragged down lower crust is expected to later partially melt and mix with the asthenosphere.

[33] Concerning the velocity of delamination, our estimated value of 4 cm yr^{-1} for the reference experiment (ranging from 0.7 to 14.6 cm yr^{-1} in others experiments), is consistent with the range of 0.3 to 8.0 cm yr^{-1} obtained by *Bird and Baumgardner* [1981] for a mantle of viscosity 10^{21} Pa s^{-1}. *Morency and Doin* [2004] found similar values, with a velocity larger than 10 cm yr^{-1} for a 590 km long sinking DLM and an asthenospheric viscosity of 10^{19} Pa s^{-1}. Our purely dynamic experiments likely lead to overestimated values of delamination velocities, amplitude of topographic response and width of the delaminated area, because thermal diffusion is not included [*Valera et al.*, 2008]. Differently from numerical models assuming a non linear rheology [*Schott and Schmeling*, 1998; *Morency and Doin*, 2004; *Göğüş and Pysklywec*, 2008b], strain localization and DLM breakoff never occur in our experiments due to the constant viscosity of the materials used here, and therefore the amplitude of depression keeps on increasing until the DLM reaches the base of the box. On the other hand, the two-dimensional approach adopted in thermal-mechanical numerical models likely leads to underestimation of velocity of delamination, since return flow around the edges of DLM (toroidal flow) is not accounted for.

4.4. Comparison With Natural Systems

[34] Despite the oversimplified experimental setting, we can try to export the modeling results to interpret the behavior of natural systems, taking

into account the limitations imposed by the adopted experimental setting (see section 2). In the following discussion we focus on a qualitative comparison with the southern Sierra Nevada range (California, USA), as a large number of observations compatible with the occurrence of delamination are found in this area. For instance, *Zandt et al.* [2004] proposed a sequential history for the evolution of the southern Sierra Nevada, based on the lateral propagation of the foundering of an ultramafic lithospheric root. *Le Pourhiet et al.* [2006] considered a completely different initial setup and proposed a delamination model in which a local instability induced a localized small-scale convection that thermally eroded the lithospheric mantle, enhancing the connection between the asthenosphere and lower crust by means of a low viscosity zone. Whatever the triggering mechanism, our setup reproduces similar scale situation. We performed experiments with a scaled lithospheric root of 42 to 83 km, present over a width of 83 to 250 km, coherent with the supposed delaminated root estimated to 40 to 70 km thick [*Ducea and Saleeby*, 1998] that probably underlain most of the ca. 100 km-wide Sierra Nevada range [*Jones et al.*, 2004]. The density contrast with the asthenosphere is estimated to 10 kg m^{-3} (from three-dimensional shear wave velocity structure [*Fay et al.*, 2008]) to 200 kg m^{-3} (from xenoliths studies [*Ducea and Saleeby*, 1998]), in the same order of magnitude as our scaled values of 23 to 100 kg m^{-3}. The presence of an adjacent weak area is generally attributed to the previous early Cenozoic subduction and could represent a fluid-weakened lithosphere by dehydration processes [*Schott and Schmeling*, 1998; *Zandt et al.*, 2004; *Valera et al.*, 2008]. Alternatively, an "asthenospheric conduit" would be more consistent with strong thermal thinning in the upper plate above the hydrated zone [*Arcay et al.*, 2007]. For simplicity, the experiments performed in this study are always characterized by free boundaries while in nature plates are laterally confined. In particular, it would imply that the plate motion recorded during the last stage of our experimental delamination is not realistic since a laterally constrained natural plate would exhibit a strong active shortening retroward of the delamination's direction, as recorded in models characterized by free-slip boundary conditions [e.g., *Schott and Schmeling* 1998]. Hence, in nature the topographic signal could also be affected by an extra uplift due to thickening of the crust.

[35] The global topographic pattern obtained in the analog models reproduces well the surface features of the Sierra Nevada region. The depression over the sinking DLM is consistent with the subsidence currently recognized in the Tulare Lake basin (southern Great Valley [*Saleeby and Foster*, 2004]). Uplift associated with poloidal flow and replacement of lithospheric mantle by more buoyant asthenosphere (Figure 10) is coherent with the recent uplift/tilting of the Sierra Nevada range [*Unruh*, 1991; *Wakabayashi and Sawyer*, 2001; *Saleeby and Foster*, 2004; *Stock et al.*, 2004; *Bennett et al.*, 2009]. The order of magnitude of both isostatic reequilibration (2 km) and dynamically uplifted bulge (1.7 to 6.7 km) obtained in laboratory (Figure 5) are similar to the estimated uplift of the Sierra >1 km [e.g., *Jones et al.*, 2004, and references therein]. However, in our models, the removal of lithosphere is preceded by strong subsidence accompanying the dynamic uplift. Though today's Great Valley fits such a pattern [*Saleeby and Foster*, 2004], there is no record of subsidence in the Sierra Nevada Range preceding its recent uplift. Deformation pattern with proward propagation of the extension front above the delaminated area (Figure 4) is consistent with the westward migration of normal faulting along the edge of the Sierra [*Jones et al.*, 2004, and references therein]. Both partial melting found in the lower crust under Sierra Nevada [*Ducea and Saleeby*, 1998], return-flow [*Boyd et al.*, 2004] and high alkaline magmatic pulse migrating over the last 4–3 Myr [*Manley et al.*, 2000] are observations compatible with our experimental study, which shows the strong upwelling and intrusion of the asthenosphere along the base of the crust (Figure 10). Mantle flow patterns imply large shear stress at the base of the lower crust. Poloidal flow injecting the lower crust will induce proward-directed shear, whereas the counterflow will produce retroward-directed shear. The seismic anisotropy fabric of the crust-mantle boundary recognized using receiver functions is interpreted to be likely caused by shearing along a detachment zone [*Zandt et al.*, 2004], which is in agreement with our modeling results.

[36] One puzzling point in the history of the Sierra Nevada is the timing of delamination. Although the presence of the eclogitic root is attested since ca. 80 My, delamination started very recently at ca. 8 My and was very rapid [*Ducea and Saleeby*, 1998; *Manley et al.*, 2000; *Wakabayashi and Sawyer*, 2001; *Jones et al.*, 2004]. In our experiments, a long initiation phase (because of a low root pull force and/or high viscosity contrast between lithosphere and asthenosphere) is always correlated with a slow process and conversely. We suggest

that the onset of delamination could be related to a change in boundary conditions or a disturbing intermediate-depth event (e.g., change in global mantle flow circulation), not reproduced in our models.

5. Conclusions

[37] The present work highlights the dynamics of continental delamination with little internal deformation and triggered by the presence of a density anomaly (lithospheric root) and a weak zone. Our results show that delamination is first controlled by coupling between lower crust and lithospheric mantle and bending resistance of the DLM during a slow initiation phase. The propensity for delamination to initiation can be empirically constrained via a parameter I representative of the ratio of driving forces over resisting forces. Delamination then evolves toward a root-pull dominated phase during which the delaminating lithospheric mantle adopts the dynamics of a Stokes' sinker. Vertical velocity and propensity for the process to stop or proceed during this second stage can be characterized by an empirical buoyancy parameter B. The induced topographic response is a combination of local isostatic reequilibration, flexural bending and dynamic topography. Especially, the onset of delamination is not marked by uplift, but by a strong dynamic subsidence above the density anomaly, associated with contraction. A poloidal mantle flow then develops around the tip of the DLM and is responsible for a strong dynamic uplift next to the delamination hinge. Ultimately, a counterflow triggers a retroward motion of the model that could induce a significant amount of shortening in constrained natural systems. Many features of our models are consistent with observations in the Sierra Nevada (overall topographic signal, migration of extension and volcanism). However, the absence of significant subsidence preceding uplift of the range and timing/duration of delamination suggest that others processes than pure density-driven detachment may have affected the Sierra Nevada and triggered delamination.

Notation

g	gravitational acceleration, m s^{-2}
h_l	thickness of the continental lithosphere, m
h_{UC}	thickness of the upper crust, m
h_{LC}	thickness of the lower crust, m
h_{LM}	thickness of the lithospheric mantle, m
h_{asth}	thickness of the upper mantle asthenosphere, m
W	width of the lithospheric root, m
H	thickness of the lithospheric root, m
w	width of the asthenospheric channel, m
w_c	critical width of the asthenospheric channel, m
ρ_l	density of the continental lithosphere, kg m^3
ρ_{UC}	density of the upper crust, kg m^3
ρ_{LC}	density of the lower crust, kg m^3
ρ_{LM}	density of the lithospheric mantle, kg m^3
ρ_{asth}	density of the asthenosphere, kg m^3
$\Delta\rho$	density contrast between lithospheric mantle and asthenosphere, kg m^3
η_l	viscosity of the continental lithosphere, Pa s^{-1}
η_{LC}	viscosity of the lower crust, Pa s^{-1}
η_{LM}	viscosity of the lithospheric mantle, Pa s^{-1}
η_{asth}	viscosity of the asthenosphere, Pa s^{-1}
τ_{LC}	shear stress at the base of the lower crust, N m^{-2}
$\dot{\gamma}$	shear rate in the lower crust, s^{-1}
v	velocity in the lower crust, m s^{-1}
V_d	horizontal velocity of delamination (hinge migration), m s^{-1}
V	mean vertical velocity of the DLM during Stokes' phase, m s^{-1}
r	radius of curvature of the lithospheric mantle expressed as deviation of the initial straight shape, m
t	duration of initiation phase, s
T	total duration of the experiment, s
$T°$	ratio of duration of initiation over total duration of the experiment
$t°$	characteristic time
$U°$	characteristic velocity
F_{rp}	root pull force, N
R_b	bending resistance of the lithospheric mantle, N m^{-1}
R_{asth}	viscous resistance at the interface DLM-asthenosphere, N m^{-1}
I	initiation parameter, s^7 m^{-3}
I_c	critical value of the initiation parameter, s^7 m^{-3}
B	buoyancy parameter, m^4 s^4 kg^{-1}
B_c	critical value of the buoyancy parameter, m^4 s^4 kg^{-1}

Acknowledgments

[38] F. Bajolet was funded by the European Union FP7 Marie Curie ITN "Crystal2Plate," contract no. 215353. J. Galeano and A. M. Negredo acknowledge support from Spanish Research Ministry projects CGL2008–04968, CGL2009–13103 and

CSD2006–00041 (TOPO-IBERIA). F. Funiciello was supported by the European Young Investigators (EURYI) Awards Scheme (Eurohorcs/ESF including funds the National Research Council of Italy). Experiments presented in this paper have been realized at the Laboratory of Experimental Tectonics, Univ. "Roma TRE," Italy. The paper benefited from constructive reviews by T. Gerya and the Editor J. Tyburczy.

References

Arcay, D., E. Tric, and M. P. Doin (2007), Slab surface temperature in subduction zones: Influence of the interplate decoupling depth and upper plate thinning processes, *Earth Planet. Sci. Lett.*, *255*(3–4), 324–338, doi:10.1016/j.epsl.2006.12.027.

Arnold, J., W. R. Jacoby, H. Schmeling, and B. Schott (2001), Continental collision and the dynamic and thermal evolution of the Variscan orogenic crustal root—Numerical models, *J. Geodyn.*, *31*(3), 273–291, doi:10.1016/S0264-3707(00)00023-5.

Bennett, R. A., N. P. Fay, S. Hreinsdottir, C. Chase, and G. Zandt (2009), Increasing long-wavelength relief across the southeastern flank of the Sierra Nevada, California, *Earth Planet. Sci. Lett.*, *287*(1–2), 255–264, doi:10.1016/j.epsl.2009.08.011.

Bird, P. (1978), Initiation of intracontinental subduction in the Himalaya, *J. Geophys. Res.*, *83*(B10), 4975–4987, doi:10.1029/JB083iB10p04975.

Bird, P. (1979), Continental delamination and the Colorado Plateau, *J. Geophys. Res.*, *84*(B13), 7561–7571.

Bird, P., and J. Baumgardner (1981), Steady propagation of delamination events, *J. Geophys. Res.*, *86*(B6), 4891–4903, doi:10.1029/JB086iB06p04891.

Boyd, O. S., C. H. Jones, and A. F. Sheehan (2004), Foundering lithosphere imaged beneath the Southern Sierra Nevada, California, USA, *Science*, *305*, 660–662, doi:10.1126/science.1099181.

Calvert, A., E. Sandvol, D. Seber, M. Barazangi, S. Roecker, T. Mourabit, F. Vidal, G. Alguacil, and N. Jabour (2000), Geodynamic evolution of the lithosphere and upper mantle beneath the Alboran region of the western Mediterranean: Constraints from travel time tomography, *J. Geophys. Res.*, *105*(B5), 10,871–10,898, doi:10.1029/2000JB900024.

Cardozo, N., and R. W. Allmendinger (2009), SSPX: A program to compute strain from displacement/velocity data, *Comput. Geosci.*, *35*(6), 1343–1357, doi:10.1016/j.cageo.2008.05.008.

Channell, J. E. T., and J. C. Mareschal (1989), Delamination and asymmetric lithospheric thickening in the development of the Tyrrhenian Rif, in *Alpine Tectonics*, edited by M. P. Coward, D. Dietrich and R. G. Park, *Geol. Soc. Spec. Publ.*, *45*, 285–302, doi:10.1144/GSL.SP.1989.045.01.16.

Chemenda, A. I., J. P. Burg, and M. Mattauer (2000), Evolutionary model of the Himalaya-Tibet system: Geopoem based on new modelling, geological and geophysical data, *Earth Planet. Sci. Lett.*, *174*(3–4), 397–409, doi:10.1016/S0012-821X(99)00277-0.

Conrad, C. P., and B. H. Hager (1999), Effects of plate bending and fault strength at subduction zones on plate dynamics, *J. Geophys. Res.*, *104*(B8), 17,551–17,571, doi:10.1029/1999JB900149.

Davies, G. F. (1980), Mechanics of subducted lithosphere, *J. Geophys. Res.*, *85*(B11), 6304–6318, doi:10.1029/JB085iB11p06304.

Davy, P., and P. R. Cobbold (1991), Experiments on shortening of a 4-layer model of the continental lithosphere, *Tectonophysics*, *188*(1–2), 1–25, doi:10.1016/0040-1951(91)90311-F.

Ducea, M., and J. Saleeby (1998), A case for delamination of the deep batholithic crust beneath the Sierra Nevada, California, *Int. Geol. Rev.*, *40*(1), 78–93, doi:10.1080/00206819809465199.

England, P., and G. Houseman (1989), Extension during continental convergence, with application to the Tibetan Plateau, *J. Geophys. Res.*, *94*(B12), 17,561–17,579, doi:10.1029/JB094iB12p17561.

Faccenda, M., G. Minelli, and T. V. Gerya (2009), Coupled and decoupled regimes of continental collision: Numerical modeling, *Earth Planet. Sci. Lett.*, *278*(3–4), 337–349, doi:10.1016/j.epsl.2008.12.021.

Faccenna, C., P. Davy, J. P. Brun, R. Funiciello, D. Giardini, M. Mattei, and T. Nalpas (1996), The dynamics of back-arc extension: An experimental approach to the opening of the Tyrrhenian Sea, *Geophys. J. Int.*, *126*(3), 781–795, doi:10.1111/j.1365-246X.1996.tb04702.x.

Faccenna, C., D. Giardini, P. Davy, and A. Argentieri (1999), Initiation of subduction at Atlantic-type margins: Insights from laboratory experiments, *J. Geophys. Res.*, *104*(B2), 2749–2766, doi:10.1029/1998JB900072.

Fay, N. P., R. A. Bennett, J. C. Spinler, and E. D. Humphreys (2008), Small-scale upper mantle convection and crustal dynamics in southern California, *Geochem. Geophys. Geosyst.*, *9*, Q08006, doi:10.1029/2008GC001988.

Fillerup, M. A., J. H. Knapp, C. C. Knapp, and V. Raileanu (2010), Mantle earthquakes in the absence of subduction? Continental delamination in the Romanian Carpathians, *Lithosphere*, *2*(5), 333–340, doi:10.1130/L102.1.

Forsyth, D., and S. Uyeda (1975), On the relative importance of the driving forces of plate tectonics, *Geophys. J. R. Astron. Soc.*, *43*(1), 163–200, doi:10.1111/j.1365-246X.1975.tb00631.x.

Funiciello, F., C. Faccenna, D. Giardini, and K. Regenauer-Lieb (2003), Dynamic of retreating slabs: 2. Insights from three-dimensional laboratory experiments, *J. Geophys. Res.*, *108*(B4), 2207, doi:10.1029/2001JB000896.

Funiciello, F., C. Faccenna, and D. Giardini (2004), Role of lateral mantle flow in the evolution of subduction systems: Insights from laboratory experiments, *Geophys. J. Int.*, *157*(3), 1393–1406, doi:10.1111/j.1365-246X.2004.02313.x.

Funiciello, F., M. Moroni, C. Piromallo, C. Faccenna, A. Cenedese, and H. A. Bui (2006), Mapping mantle flow during retreating subduction: Laboratory models analyzed by feature tracking, *J. Geophys. Res.*, *111*, B03402, doi:10.1029/2005JB003792.

Funiciello, F., C. Faccenna, A. Heuret, S. Lallemand, E. Di Giuseppe, and T. W. Becker (2008), Trench migration, net rotation and slab-mantle coupling, *Earth Planet. Sci. Lett.*, *271*(1–4), 233–240, doi:10.1016/j.epsl.2008.04.006.

Gîrbacea, R., and W. Frisch (1998), Slab in the wrong place: Lower lithospheric mantle delamination in the last stage of the eastern Carpathian subduction retreat, *Geology*, *26*(7), 611–614, doi:10.1130/0091-7613(1998)026<0611:SITWPL>2.3.CO;2.

Göğüş, O. H., and R. N. Pysklywec (2008a), Mantle lithosphere delamination driving plateau uplift and synconvergent extension in eastern Anatolia, *Geology*, *36*(9), 723–726, doi:10.1130/G24982A.1.

Göğüş, O. H., and R. N. Pysklywec (2008b), Near-surface diagnostics of dripping or delaminating lithosphere, *J. Geophys. Res.*, *113*, B11404, doi:10.1029/2007JB005123.

Göğüş, O. H., R. N. Pysklywec, F. Corbi, and C. Faccenna (2011), The surface tectonics of mantle lithosphere delamination following ocean lithosphere subduction: Insights from physical-scaled analogue experiments, *Geochem. Geophys. Geosyst.*, *12*, Q05004, doi:10.1029/2010GC003430.

Griffiths, R. W., R. I. Hackney, and R. D. van der Hilst (1995), A laboratory investigation of effects of trench migration on the descent of subducted slabs, *Earth Planet. Sci. Lett.*, *133*(1–2), 1–17, doi:10.1016/0012-821X(95)00027-A.

Guillou-Frottier, L., J. Buttles, and P. Olson (1995), Laboratory experiments on the structure of subducted lithosphere, *Earth Planet. Sci. Lett.*, *133*(1–2), 19–34, doi:10.1016/0012-821X(95)00045-E.

Houseman, G., D. McKenzie, and P. Molnar (1981), Convective instability of a thickened boundary layer and its relevance for the thermal evolution of continental convergent belts, *J. Geophys. Res.*, *86*(B7), 6115–6132, doi:10.1029/JB086iB07p06115.

Jacoby, W. R. (1980), Plate sliding and sinking in mantle convection and the driving mechanism, in *Mechanisms of Continental Drift and Plate Tectonics*, edited by P. A. Davis and F. R. S. Runcorn, pp. 159–172, Academic, London.

Jones, C. H., G. L. Farmer, and J. Unruh (2004), Tectonics of Pliocene removal of lithosphere of the Sierra Nevada, California, *Geol. Soc. Am. Bull.*, *116*(11), 1408–1422, doi:10.1130/B25397.1.

Kincaid, C., and P. Olson (1987), An experimental-study of subduction and slab migration, *J. Geophys. Res.*, *92*(B13), 13,832–13,840, doi:10.1029/JB092iB13p13832.

Knapp, J. H., C. C. Knapp, V. Raileanu, L. Matenco, V. Mocanu, and C. Dinu (2005), Crustal constraints on the origin of mantle seismicity in the Vrancea zone, Romania: The case for active continental lithospheric delamination, *Tectonophysics*, *410*(1–4), 311–323, doi:10.1016/j.tecto.2005.02.020.

Lallemand, S., A. Heuret, C. Faccenna, and F. Funiciello (2008), Subduction dynamics as revealed by trench migration, *Tectonics*, *27*, TC3014, doi:10.1029/2007TC002212.

Lastowka, L. A., A. F. Sheehan, and J. M. Schneider (2001), Seismic evidence for partial lithospheric delamination model of Colorado Plateau uplift, *Geophys. Res. Lett.*, *28*(7), 1319–1322, doi:10.1029/2000GL012360.

Le Pourhiet, L., M. Gurnis, and J. Saleeby (2006), Mantle instability beneath the Sierra Nevada mountains in California and Death Valley extension, *Earth Planet. Sci. Lett.*, *251*(1–2), 104–119, doi:10.1016/j.epsl.2006.08.028.

Levander, A., B. Schmandt, M. S. Miller, K. Liu, K. E. Karlstrom, R. S. Crow, C. T. A. Lee, and E. D. Humphreys (2011), Continuing Colorado plateau uplift by delamination-style convective lithospheric downwelling, *Nature*, *472*, 461–465, doi:10.1038/nature10001.

Manley, C. R., A. F. Glazner, and G. L. Farmer (2000), Timing of volcanism in the Sierra Nevada of California: Evidence for Pliocene delamination of the batholithic root?, *Geology*, *28*(9), 811–814, doi:10.1130/0091-7613(2000)28<811:TOVITS>2.0.CO;2.

McKenzie, D. (1977), The initiation of trenches: A finite amplitude instability, in *Island Arcs, Deep Sea Trenches and Back-Arc Basins*, *Maurice Ewing Ser.*, vol. 1, edited by M. Talwani and W. C. Pitman III, pp. 57–61, AGU, Washington, D. C., doi:10.1029/ME001p0057.

Morency, C., and M. P. Doin (2004), Numerical simulations of the mantle lithosphere delamination, *J. Geophys. Res.*, *109*, B03410, doi:10.1029/2003JB002414.

Pysklywec, R. N., and A. R. Cruden (2004), Coupled crust-mantle dynamics and intraplate tectonics: Two-dimensional numerical and three-dimensional analogue modeling, *Geochem. Geophys. Geosyst.*, *5*, Q10003, doi:10.1029/2004GC000748.

Saleeby, J., and Z. Foster (2004), Topographic response to mantle lithosphere removal in the southern Sierra Nevada region, *Calif. Geol.*, *32*(3), 245–248, doi:10.1130/g19958.1.

Schellart, W. P. (2004), Kinematics of subduction and subduction-induced flow in the upper mantle, *J. Geophys. Res.*, *109*, B07401, doi:10.1029/2004JB002970.

Schott, B., and H. Schmeling (1998), Delamination and detachment of a lithospheric root, *Tectonophysics*, *296*(3–4), 225–247, doi:10.1016/S0040-1951(98)00154-1.

Seber, D., M. Barazangi, A. Ibenbrahim, and A. Demnati (1996), Geophysical evidence for lithospheric delamination beneath the Alboran Sea and Rif-Betic mountains, *Nature*, *379*, 785–790, doi:10.1038/379785a0.

Stock, G. M., R. S. Anderson, and R. C. Finkel (2004), Pace of landscape evolution in the Sierra Nevada, California, revealed by cosmogenic dating of cave sediments, *Geology*, *32*(3), 193–196, doi:10.1130/G20197.1.

Turcotte, D. L., and G. Schubert (1982), *Geodynamics Application of Continuum Physics to Geological Problems*, 450 pp., John Wiley, New York.

Unruh, J. R. (1991), The uplift of the Sierra-Nevada and implications for Late Cenozoic epeirogeny in the Western Cordillera, *Geol. Soc. Am. Bull.*, *103*(11), 1395–1404, doi:10.1130/0016-7606(1991)103<1395:TUOTSN>2.3.CO;2.

Valera, J. L., A. M. Negredo, and A. Villasenor (2008), Asymmetric delamination and convective removal numerical modeling: Comparison with evolutionary models for the Alboran Sea Region, *Pure Appl. Geophys.*, *165*(8), 1683–1706, doi:10.1007/s00024-008-0395-8.

Valera, J. L., A. M. Negredo, and I. Jimenez-Munt (2011), Deep and near-surface consequences of root removal by asymmetric continental delamination, *Tectonophysics*, *502*(1–2), 257–265, doi:10.1016/j.tecto.2010.04.002.

Wakabayashi, J., and T. L. Sawyer (2001), Stream incision, tectonics, uplift, and evolution of topography of the Sierra Nevada, California, *J. Geol.*, *109*(5), 539–562, doi:10.1086/321962.

Weijermars, R., and H. Schmeling (1986), Scaling of Newtonian and non-Newtonian fluid dynamics without inertia for quantitative modeling of rock flow due to gravity (including the concept of rheological similarity), *Phys. Earth Planet. Inter.*, *43*, 316–330, doi:10.1016/0031-9201(86)90021-X.

Zandt, G., H. Gilbert, T. J. Owens, M. Ducea, J. Saleeby, and C. H. Jones (2004), Active foundering of a continental arc root beneath the southern Sierra Nevada in California, *Nature*, *431*, 41–46, doi:10.1038/nature02847.